SSSAJ

SOIL SCIENCE SOCIETY OF AMERICA JOURNAL

Vol. 79 • No. 04
July–August 2015

SSJO4

Published July 24, 2015

From Real Soils to 3D-Printed Soils: Reproduction of Complex Pore Network at the Real Size in a Silty-Loam Soil

N. Dal Ferro
F. Morari*
Dep. of Agronomy, Food, Natural resources, Animals and Environment
Agripolis
Univ. of Padova
Viale Dell'Università 16
35020 Legnaro (Padova)
Italy

Pore complexity and micro-heterogeneity are pivotal in characterizing biogeochemical processes in soils. Recent advances in X-ray computed microtomography (microCT) allow the 3D soil morphology characterization of undisturbed samples, although its geometrical reproduction at very small spatial scales is still challenging. Here, by combining X-ray microCT with 3D multijet printing technology, we aimed to evaluate the reproducibility of 3D-printing soil structures at the original scale with a resolution of 80 μm and compare the hydraulic properties of original soil samples with those obtained from the soil-like prototypes. Results showed that soil-like prototypes were similar to the original samples in terms of total porosity and pore shape. By contrast the pore connectivity was reduced by incomplete wax removal from pore cavities after the 3D printing procedure. Encouraging results were also obtained in terms of hydraulic conductivity since measurements were successfully conducted on five out of six samples, showing positive correlation with experimental data. We are confident that future developments of 3D-printing technologies and of their combination with microCT will help to further the understanding of soil micro-heterogeneity and its effects on soil-water dynamics.

Abbreviations: C, control; M, manure at 60 Mg ha^{-1}; microCT, computed microtomography; PSD, pore-size distribution; STL, Standard Tresellation Language; 500k, 500 000; 10M, 10 Million.

The processes that form porous media lead to highly heterogeneous 3D structures, forcing scientists to adopt models for reproducing the reality. This is the case for soil physics, which has its foundations laid on the capillary bundle model (Hunt et al., 2013). Water flow is still commonly conceptualized as a 2D bundle of cylindrical tubes passing through the soil only in the vertical direction, trivializing the natural complexity of a soil. As a result, derived models such as those of water conductivity (Burdine, 1953; Mualem, 1976) introduced empirical adjustments (e.g., a tortuosity factor) to compensate for fundamental errors in the conceptual model (Hunt et al., 2013). The simplification of reality in 1D or 2D models was supported by the inability to see and understand the 3D structure and its interactions with biota due to its opaque nature (Feeney et al., 2006). However, recent advanced technologies have provided a vast amount of data and their assimilation in more complex models that have partly superseded the use of reduction methods (Ahuja et al., 2006). The first steps for creating real-world situations in soil science used 3D random network models (e.g., Rajaram et al., 1997; Peat et al., 2000) that mimicked the soil complexity and dynamics in a 3D space. In spite of their overall improvement in the understanding of matrix flow and transport of solutes, these models had two main limitations: 1. Computing limitations make some structural simplification unavoidable. 2. The soil has such structural complexity that a reliable estimate of a representative elementary volume is dif-

Soil Sci. Soc. Am. J. 79:1008–1017
doi:10.2136/sssaj2015.03.0097
Received 11 Mar. 2015.
Accepted 11 May 2015.
*Corresponding author (Francesco.morari@unipd.it).

Table 1. Texture and computed microtomography (microCT) pore morphological parameters of original soil cores (4.8 cm high × 4.8 cm diam.). Standard error values are reported in brackets.

		Soil physical properties				MicroCT parameters			
ID	Replicate	Sand	Silt	Clay	Total porosity†	MicroCT porosity	Mean pore diameter‡	Pore surface/volume	Euler number
			%			$m^3\ m^{-3}$	μm	μm^{-1}	mm^{-3}
M	1	32.1	63.3	4.7	0.490	0.086	783.74	0.008	0.31
M	2	32.0	63.3	4.7	0.461	0.102	530.24	0.011	1.09
M	3	30.0	65.0	5.0	0.476	0.045	883.97	0.009	0.16
Average		31.4(0.7)	63.9(0.6)	4.8(0.1)	0.476(0.008)	0.078(0.017)	732.65(105.26)	0.009(0.001)	0.52(0.29)
C	1	27.5	65.7	6.7	0.459	0.015	386.96	0.011	0.16
C	2	37.8	57.2	5.0	0.432	0.020	338.58	0.014	0. 6
C	3	32.6	62.0	5.4	0.439	0.033	374.06	0.013	3.13
Average		32.6(3.0)	61.6(2.5)	5.7(0.5)	0.443(0.008)	0.023(0.005)	366.53(14.46)	0.013(0.001)	1.65(1.21)

†Gravimetric method with water saturation.

‡Weighted mean of soil pore-size distribution.

ficult to quantify (Peat et al., 2000), as for most of the models. Lately, non-invasive imaging approaches have gained attention as they provide the opportunity to examine soil–water interactions from direct observations at the microscale. For example, the soil physical and chemical processes were replicated using high-tech materials with a refractive index similar to water, allowing the use of 3D optical microscopy in a transparent-reconstructed medium for the visualization of biophysical processes. Controlled experiments of how pore channels can influence the biological and hydraulic dynamics can be realized, although the reconstructed medium is only partially reproducible because it is composed of single incoherent particles (Downie et al., 2012).

Impressive developments and insights into porous media research have also been provided by X-ray microCT that allows microscopic visualization of the spatial arrangement of complex structures (Cnudde and Boone, 2013). For the first time it became possible to investigate the interior of an object in a nondestructive way and to extract qualitative and quantitative information of multiphase porous materials (e.g., Tippkoetter et al., 2009; Mooney et al., 2012). In this context "digital rock physics", that is, the study of pore scale processes by the use of digital imaging and modeling, has expanded enormously the understanding of single and multiphase flow dynamics (Blunt et al., 2013).

Only recently 3D-printers have gained attention in the design of niche products, prototypes, and one-time creations (e.g., Rangel et al., 2013), although the technology is 30-yr old. This technology has been proposed in research as a tool to integrate virtual microCT information with real building models. In fact, the combination of such techniques make it possible to reconstruct complex microcosms with the heterogeneity discovered with microCT at a resolution of few micrometers, providing the opportunity to isolate the physical and chemical aspects that govern the biogeochemical and microbial processes in the soil (Otten et al., 2012; Ju et al., 2014; Bacher et al., 2015; Ringeisen et al., 2015). Nowadays, with 3D printing the diversified geometry encountered in a soil can be replicated at a resolution of tends of micrometers. Several materials can be used including plastics, resins, ceramics, and metals.

Despite large uncertainties persisting about soil microscale heterogeneity and its effects on the macroscopic dynamics (Baveye et al., 2011), so far few have tried to combine high-resolution 3D imaging and printing technology to improve knowledge in soil science. In this study we combined 3D printing technology with X-ray microCT in an attempt to reconstruct the 3D complexity of the soil structure in a soil-derived model at the same spatial scale as the original one and test some hydraulic properties.

MATERIAL AND METHODS

Experimental Design and Soil Sampling

The soil samples come from a long-term experiment established in 1962 at the experimental farm of the University of Padova (Italy). The soil (Table 1) is Fluvi-Calcaric Cambisol (CMcf), silty loam (FAO-UNESCO, 1990). This work considered soil samples from a long-term trial that compares two treatments: farmyard manure at 60 Mg ha^{-1} yr^{-1} (hereafter labeled M) and a no fertilization control (hereafter labeled C) on a continuous maize crop system. The same type of tillage has been used for both treatments, with autumn plowing and subsequent cultivations before sowing the main crop. The experimental layout is a randomized block with three replicates, on plots of 7.8 × 6 m. Further details on experimental design are extensively reported in the literature (e.g., Morari et al., 2006). A total of six undisturbed soil cores (5 cm diam., 6 cm length) were collected in August 2010 (Fig. 1, Step A), at the end of the maize season, from the topsoil (5- to 20-cm depth) in polymethylmethacrylate (PMMA) cylinders using a manual hydraulic core sampler (Eijkelkamp, The Netherlands). Cores were stored at 5°C until analysis.

Computed Microtomography Soil Scanning and Image Processing

The pore structure of soil cores, labeled M_{soil} and C_{soil} for farmyard manure and no fertilization control, respectively (Fig. 1, Step B) was sampled using X-ray microCT. To allow the scanning of the whole soil core at a fine resolution, samples were analyzed at the "3S-R" facility in Grenoble (http://www.3sr-grenoble.fr/ verificd 9 June 2015) at a spatial resolution of 40 μm. Setting parameters were 100 kV, 300 μA and projections were collected during a 360° sample rotation at 0.3° angular incremental step. Each projection was the mean of 10 acquisitions and scan frequency was 7 images s^{-1}. Beam hardening artifacts were

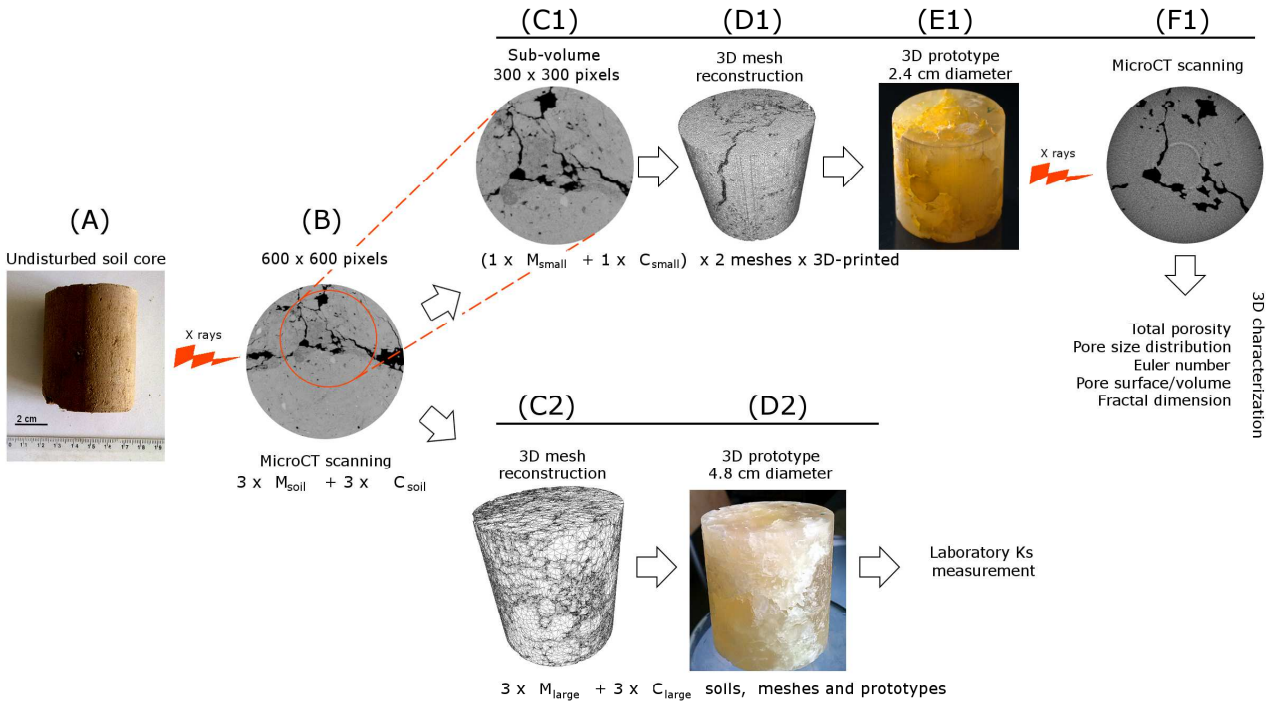

Fig. 1. Outline of steps used to obtain soil-like prototypes and sample measurements.

minimized during data acquisition using a 0.5-mm Al filter. To avoid pixel misclassification that might occur during projection measurements due to scattered radiation, nonlinearity of data acquisition systems, partial volume effects etc. (Hsieh, 2009), 2D projections were resized after acquisition using a mean filter by a two-pixel factor along the vertical and horizontal axis. As a result, the reconstructed images had a coarser resolution than that of acquisition (i.e., 80 µm). Resized projections were finally reconstructed using the dedicated software DigiCT 1.1 (Digisens, France) to obtain a stack of about 750 2D slices in 32-bit depth. The 32-bit images were later converted into 8-bit depth.

The digital image processing and analysis of soil samples, conducted with the public domain image processing ImageJ (Vs. 1.45, National Institute of Health, http://rsb.info.nih.gov/ij), has already been reported in (Dal Ferro et al., 2013). Briefly, a cylindrical volume of interest with a diameter of 600 pixels and composed of 600 slices (4.8 cm height × 4.8 cm diam.) was selected to exclude the PMMA sample holder. Slices were segmented using a global-threshold value based on the histogram greyscale that was determined by the maximum entropy threshold algorithm. The threshold value was selected where the inter-class entropy was maximized (Luo et al., 2010). Eight-connectivity, a mathematical morphology closing operator (Serra, 1982), was applied to the binary images to fill misclassified pixels inside the pores as well as to maintain pore connections (Mooney et al., 2006). Successively, the one interconnected pore network (infinite cluster) that contained most of the porosity within each stack was extracted and analyzed with CTAn software v. 1.12.0.0 (Bruker micro-CT, Kontich, Belgium) as this pore space was the only one to show continuity between the top and bottom of the soil cores. Although more connections between pores were likely present within the soil cores, microCT imaging provided only connections larger than the resolution limits, restricting our analysis to the soil macroporosity. A description of the soil morphological parameters as a result of microCT scanning has already been reported in Dal Ferro et al. (2015) (Table 1).

3D Mesh Generation

A surface mesh model for each sample (3 replicates × 2 treatments) was extracted from the one interconnected pore network that was identified from the microCT stacks using the free software InVesalius 3.0 (CTI, Campinas, São Paulo, Brazil) (Fig. 1, Step G). The created model was then exported in the geometrical stereolithography file format encoded in Standard Tessellation Language (STL). The reconstructed STL model, composed of 10 to 30 million triangles depending on the complexity of the pore network, was visualized with the open-source software MeshLab v.1.3.2 (STI-CNR, Rome, Italy; http://meshlab.sourceforge.net/; verified 9 June 2015) to assess the continuity of pore connections along the vertical axis and successively simplified to a polygonal mesh that consisted of up to 10 million triangles. To compare the microCT imaging from the original samples with the 3D-printed prototypes from the STL model, one of the three replicate microCT stacks was selected for both M and C. Afterward a volume of interest, corresponding to a cylinder of 300 pixels height × 300 pixels of diameter (Fig. 1, Step C), was extracted by both samples (2.4 cm high × 2.4-cm diam.). InVesalius 3.0 was used to obtain a polygonal mesh model, from which a STL file was exported (Fig. 1, Step D). MeshLab v.1.3.2 was used to simplify the polygonal mesh at two levels of detail, corresponding to 500 thousand (500k) and 10 million (10M) triangles, respectively. Each model was 3D-printed twice (Fig. 1,

Step E), resulting in a total of eight models (2 soil samples × 2 generated meshes × 2 replicate printings). All the closed pores, that is, the pores that had no connection to the space outside, were then digitally removed from the stacks since they cannot contribute to flow properties of the model.

3D Printing

Lastly, 14 polygonal meshes (6 cylinders, 4.8 cm h × 4.8 cm diam.; 8 cylindrical subsamples, 2.4 cm h × 2.4 cm diam.) were built with a commercial 3D printer. The printer (ProJet 3510 HD, 3D Systems, http://www.3dsystems.com/) was selected as it provided a fast prototype reconstruction with high resolution and available at a relatively low price (few hundred €). The 3D structure was printed with resin whose exact composition is proprietary but approximately contained an organic mixture of: ethoxylated bisphenol A diacrylate (15–35%, w/w), urethane acrylate oligomers (20–40%, w/w), tripropyleneglycol diacrylate (1.5–3%, w/w) (Visijet Crystal, EX 200 Plastic material, Safety Data Sheet, http://www.3dsystems.com). The 3D printer has a multijet printing technology, that is, an inkjet printing process that deposits either photocurable plastic resin or casting wax materials layer by layer, with a spatial resolution of 29 μm and a declared accuracy of 25 to 50 μm, depending on building parameters and prototype size and geometry. The final result was a set of solid prototypes whose pores were filled with paraffin wax (the contact angle between water and wax, measured with a goniometer, was 120°), while the soil matrix was composed of the resin. The contact angle between the pure resin (cleaned of any wax) and the water, measured with a contact angle goniometer, was 69°.

Wax Removal Procedure

Wax removal is crucial to empty the pores and accurately replicate the complex geometry of the soil samples. Ultrasonication in oil at a temperature of 60°C and 60 Hz for 24 h and oven drying at 60°C until stabilized weight (~4 d) were adopted as possible procedures to empty the pores. Alternative methods were considered: the use of xylene or vapor steam cleaning would have dissolved the wax, although it would have probably corrupted the solid pore surface, while alternative printing technologies without the use of wax as a physical support during 3d printing were not feasible. As a result, we adopted a simple and relatively low-cost combination between 3D printing technology and cleaning procedure.

3D Prototypes Scanning, Image Reconstruction, and Analysis

The resulting prototypes from the sub-volume of the samples (i.e., M_{small} and C_{small} at a detail of 500k and 10M triangles) were finally subjected to X-ray microCT scanning (Fig. 1, Step F) to assess: a) the reproducibility and reliability of the 3D printing process; b) the smoothing effect of polygon reduction on the generated 3D structure; c) efficacy of the cleaning procedure to remove the wax from the pores. Prototypes were analyzed with a Skyscan 1172 X-ray microtomography (Bruker micro-CT, Kontich, Belgium) at the University of Padova since lower energy than those used for scanning the whole soil sample was required to penetrate the specimen. Setting parameters were 40 kV, 250 mA and projections were collected during a 180° sample rotation at 0.25° angular incremental step. Each projection was the mean of eight acquisitions and scan frequency was 1.33 images s^{-1}. Beam hardening artifacts were minimized during data acquisition using a 0.5-mm Al filter. The spatial resolution was 27 μm. To avoid pixel misclassification that might occur during image acquisition (Hsieh, 2009), projections were resized after acquisition using a mean filter by a two-pixel factor along the vertical and horizontal axis. As a result, the reconstructed images had a final resolution twice that of acquisition (i.e., 54 μm). Resized projections were reconstructed using the dedicated software NRecon v. 1.6.9.4 provided by Bruker micro-CT to obtain a stack of about 450 2D slices in 16-bit depth. The 16-bit images were later converted into 8-bit depth.

Prototype matrix, wax, and void phases were easily visualized and binarized with a single threshold level. Eight-connectivity was applied to the binary images to fill misclassified pixels inside the pores as well as to maintain pore connections (Mooney et al., 2006). MicroCT porosity ($m^3\ m^{-3}$), PSD and open porosity (%), pore surface to volume ratio (μm^{-1}), 3D fractal dimension, and Euler number (mm^{-3}) were estimated from each binarized stack using CTAn and compared with soil parameters obtained from the original sub-volume samples.

Hydraulic Conductivity Test on 3D-Printed Prototypes

Saturated hydraulic conductivity ($K_{s\text{-}large}$) measurements were conducted on the large prototypes (M_{large} and C_{large}, 4.8 cm high × 4.8 cm diam.) (Fig. 1, Step H) by using a laboratory permeameter (Eijkelkamp, The Netherlands) that was adjusted to the size of the samples by using a gasket whose thickness created a seal at the interface between the prototype and the sample holder. $K_{s\text{-}large}$ was determined with both constant and variable head method, according to the hydraulic properties of the medium. As a rule of thumb, $K_{s\text{-}large}$ values > 5.8×10^{-6} m s^{-1} were easily determined by the constant head method, while the falling head method was conducted at smaller $K_{s\text{-}large}$ values. Before conducting the analysis and to ensure that water flowed only vertically from the top to the bottom of the prototypes, avoiding the loss of water from lateral pores, samples were first sealed with a plastic tape and successively coated with a layer of melted wax. As a result, it was ensured the complete sealing of the samples avoiding the lateral occlusion of interior pores. Successively samples were freely upward saturated at atmospheric pressure (water bath reached 3/4 of sample height) using de-aerated water, then subjected to 0.6×10^{-5} Pa to completely de-aerate them and saturated again as above.

Hydraulic Conductivity Test on Original Samples

Saturated water conductivity on soil-like prototypes was compared with water flow calculated on the original soil sam-

ples and already proposed in (Dal Ferro et al., 2015). As a result, original samples were subjected to saturated water conductivity analyses ($K_{s\text{-}soil}$, m s^{-1}) using the constant head or falling head method, depending on the soil properties and range of $K_{s\text{-}soil}$ that can be measured (Reynolds et al., 2002). In addition, the microCT imaging dataset of the original samples (scanned at the "3S-R" facility in Grenoble) was used to calculate water conductivity on the one interconnected pore cluster (K_{Morph}, m s^{-1}) by using a morphologic approach as proposed by Elliot et al. (2010). Briefly, the model consisted of combining 3D pore shape parameters with pore volume and using a modified Poiseuille equation as follows:

$$Q = \frac{\pi R^4 \Delta P}{8 L_c \nu} \quad [1]$$

where R is pore radius, ν is the viscosity of water at room temperature, DP is the change in hydrostatic pressure and L_c is the pore length, depending on pore shape characteristics.

Lastly, rearrangement of Darcy's law allowed the K_{Morph} estimation for the extracted pore network:

$$K = \frac{QL}{A \Delta P} \quad [2]$$

where A is the cross-sectional area of the sample and L is the sample length. A detailed description of the methods and results for the soils proposed here can be found in Dal Ferro et al. (2015).

RESULTS

Soil Volume and Prototype Measurements

Ultrasonication in oil was only partially able to remove the wax from pores, while the subsequent oven drying at 60°C was able to remove most of it (Fig. 2). A further increase in temperature was not possible because, according to the manufacturer, it would have weakened the resin structure or melted part of it. As a result, the combination of both techniques was used as the best procedure currently available to successfully empty the open pores as well as maintain the solid structure. However, the continuing advances in 3D-printing technology and the use of heat-resistant materials will allow the full removal of the support material (e.g., by evaporation).

Soil porosity of subvolumes scanned with microCT (M_{soil} and C_{soil} 2.4 cm high × 2.4 cm diam.) was entirely connected to the space outside the soil matrix (open pores/total porosity = 100%), but highly different between M_{soil} (0.114) and C_{soil} (0.036) (Table 2). The open pores of M_{small} prototypes were slightly lower than porosity detected by microCT, with negligible changes between 500k and 10M triangle meshes. Indeed, only 2.4% of microCT porosity (0.109 and 0.110 in 500k and 10M, respectively) was confined within the solid phase (Table 2). By contrast, the C_{small} prototypes showed a consistent increase of confined pores with respect to the total ones, ranging from 15.1% in the 500k to 18.4% in the 10M meshes, on average. As a result, the C_{soil} porosity (0.036) was slightly greater than C_{small} built both from 500k (0.024) and 10M (0.027) triangle meshes, respectively.

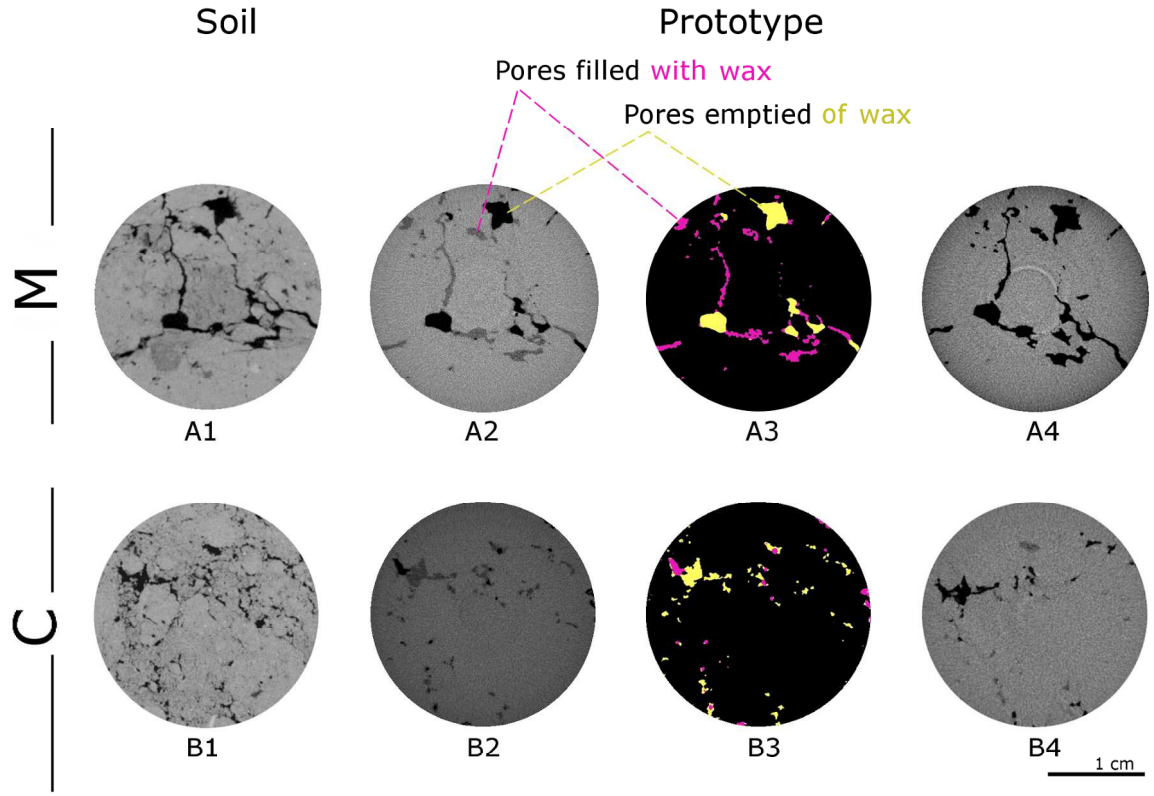

Fig. 2. Two-dimensional slices from computed microtomography (microCT) imaging (M = farmyard manure; C = control) of original soil samples (A1, B1) and soil-like prototypes after the wax removal procedure with ultrasonication (A2, A3, B2, B3) and oven drying (A4, B4).

Table 2. Three-dimensional parameters from microCT scanning of original soil volumes (M_{soil} and C_{soil}) and soil-like prototypes (M_{small} and C_{small}). Soil and soil-like volumes were 2.4 cm high × 2.4 cm diam. Standard error values are reported in brackets.

ID	Sample scanned	Mesh†	MicroCT porosity	Open pores/total porosity	Mean pore diameter‡	Pore surface/volume	Euler number	3D fractal dimension
			$m^3\ m^{-3}$	%	μm	μm^{-1}	mm^{-3}	
M_{soil}	Soil	–	0.114	100.00	858.60	0.007	0.42	2.41
M_{small}	Prototype	500k	0.113	98.97	925.60	0.007	3.54	2.61
M_{small}	Prototype	500k	0.106	96.36	943.26	0.007	0.82	2.10
M_{small}	Prototype	10M	0.113	98.71	940.04	0.007	1.70	2.62
M_{small}	Prototype	10M	0.107	96.32	953.31	0.007	0.97	2.17
Average	Prototype	–	0.110 (0.002)	97.591(0.84)	940.55(6.62)	0.007(0.000)	1.758(0.72)	2.38(0.16)
C_{soil}	Soil	–	0.036	100.00	319.02	0.014	0.33	2.25
C_{small}	Prototype	500k	0.027	90.30	397.66	0.013	0.981	2.40
C_{small}	Prototype	500k	0.022	79.59	393.33	0.013	0.171	2.55
C_{small}	Prototype	10M	0.028	86.35	380.00	0.013	0.795	2.38
C_{small}	Prototype	10M	0.025	76.90	246.21	0.026	1.509	2.46
Average	Prototype	–	0.026(0.002)	83.28(3.54)	354.30(41.83)	0.016(0.004)	0.864(0.319)	2.45(0.04)

†500k = 500 thousand tringle mesh; 10M = 10 million triangle mesh.

‡Weighted mean of soil-like prototypes pore-size distribution.

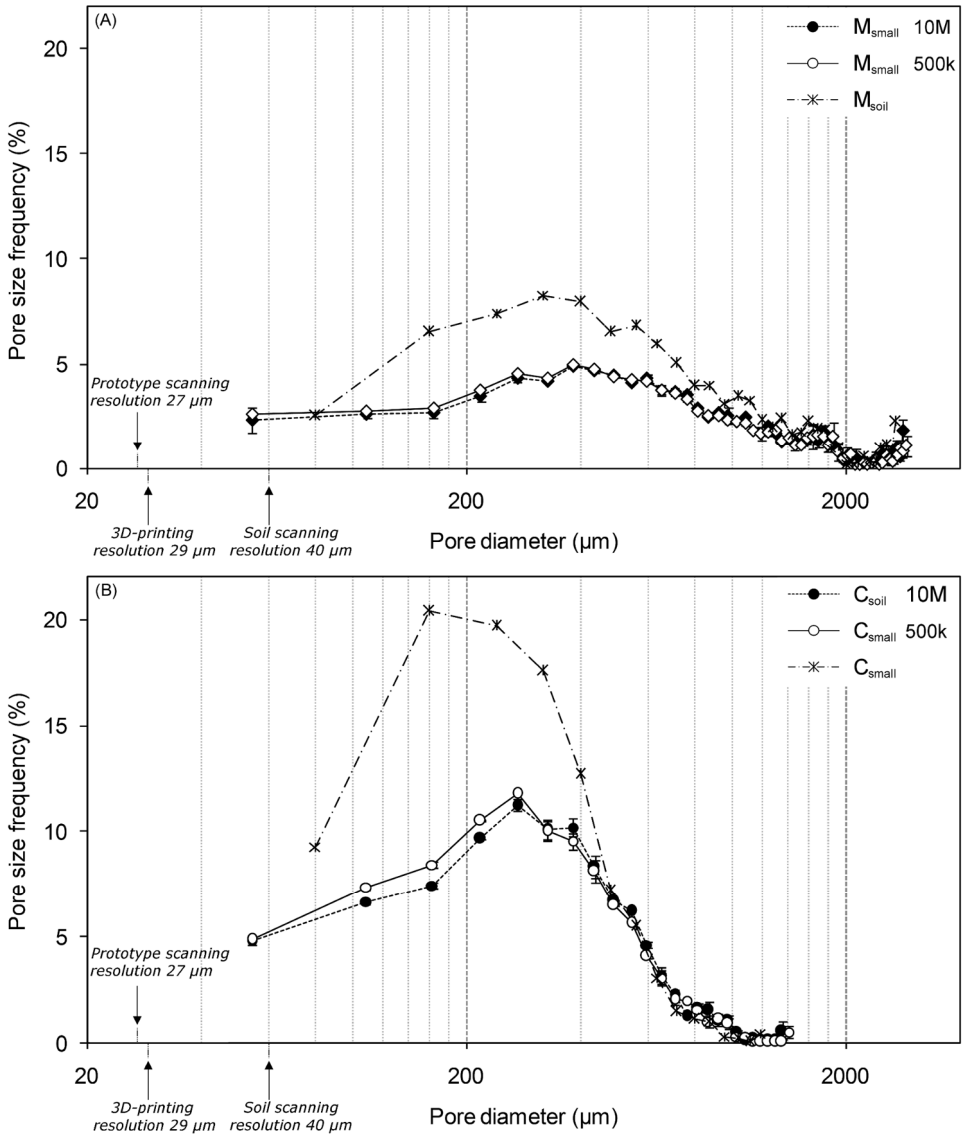

Fig. 3. Pore-size distribution estimated by means of X-ray computed microtomography (microCT) on original soil samples (M_{soil} and C_{soil}) and on soil-like prototypes (M_{small} and C_{small}) from 3D printing at different mesh accuracy (500k = 500 thousand triangles; 10M = ten million triangles).

Pore-size distribution (PSD) curves (Fig. 3), measured on microCT images in volumetric terms according to the medial-axes determination and sphere-fitting measurement (Remy and Thiel, 2002), were distributed differently between M and C. In M the most frequent pore classes were distributed between 240- and 560-μm diam., while they were shifted toward smaller pores in C, ranging between 160 and 440 μm. Comparable data were found between PSD prototype classes, in both M and C, with negligible variations between replicates and meshes. By contrast, a sharp increase of the small pores was observed in the original samples with respect to the prototypes: this was particularly clear for pore classes smaller than 800 and 490 μm in M_{soil} and C_{soil}, where the integral of the PSD differences was around 30 and 10% of microCT porosity, respectively. Finally, it was noticed that some pores were still filled with wax despite its melting and removal with ultrasonication and oven drying (Fig. 4). In particular, wax most resided in thin throats (<200 μm, on average) between largest cavities, leading to their disconnection and thus increasing both the average size of empty pores and the number of isolated ones.

Pore morphological features (Table 2), estimated by means of pore surface/volume ratio (μm^{-1}), Euler number (i.e., an indicator of pore connectivity, where the greater is the value, the lower is the pore connectivity; mm^{-3}; Vogel et al., 2010) and 3D fractal dimension (box-counting method) (Perret et al., 2003), emphasized the self-similarity between the prototypes that were generated by the same original sub-volume. For instance, the pore surface/volume ratio was 0.007 μm^{-1} in M_{small} prototypes as characterized by different meshes (500k and 10M triangles), while the fractal dimension (2.42 and 2.25 in the original M_{soil} and C_{soil}, respectively) ranged in M_{small} between 2.10 (500k triangles) and 2.62 (10M triangles) and in C_{small} between 2.38 (500k triangles) and 2.55 (10M triangles). Only the Euler number parameter, particularly in M_{small} and C_{small} built from 500k triangle meshes, showed high variability between the prototypes (Table 2).

Experimental Saturated Hydraulic Conductivity Measurements on Large Prototypes

Experimental saturated hydraulic conductivity ($K_{s\text{-}large}$) data were obtained on five of the six reconstructed large prototypes (M_{large} and C_{large} 4.8 cm high × 4.8 cm diam., an example is reported in Fig. 5) since water did not flow through one of the C_{large} samples (Table 3). The $K_{s\text{-}large}$ was generally higher in M (61.63×10^{-6} m s^{-1}, on average) than C (0.35×10^{-6} m s^{-1}, on average), ranging between a minimum of 0.23×10^{-6} m s^{-1} observed in C and a maximum of 134.9×10^{-6} m s^{-1} in M. The water flow measurements on the prototypes were generally greater (37.1×10^{-6} m s^{-1}, on average) than those measured ($K_{s\text{-}soil} = 3.59 \times 10^{-6}$, on average) and modelled ($K_{Morph} = 1.91 \times 10^{-6}$ m s^{-1}) on the original soil samples (Table 3; Dal Ferro et al., 2015). Finally, positive correlations were observed between soil-like $K_{s\text{-}large}$ values and both $K_{s\text{-}soil}$ (R^2 = 0.69) and K_{Morph} (R^2 = 0.93, Fig. 6).

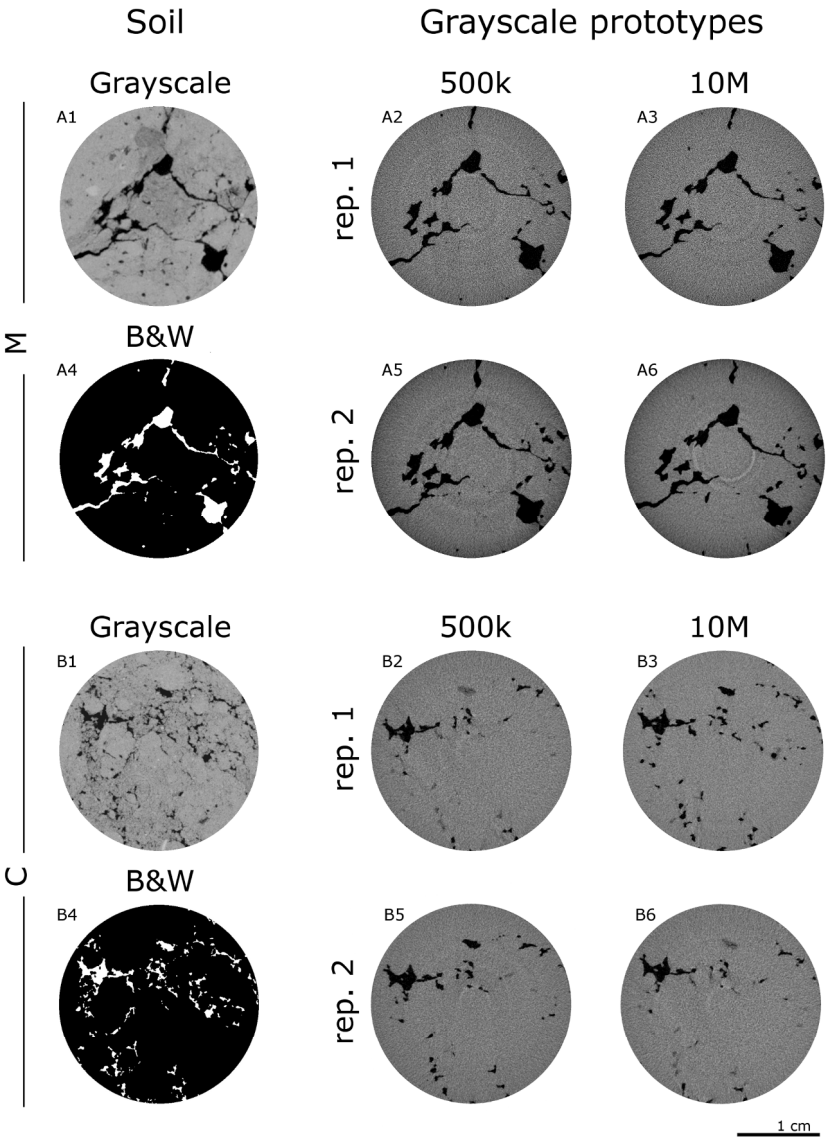

Fig. 4. Two-dimensional slices from computed microtomography (microCT) imaging of original soil samples (A1, B1) and soil-like prototypes (M = farmyard manure; C = control). Prototypes were obtained in duplicate from a polygonal mesh composed of both 500 thousand (500k; A2, A5, B2, B5) and 10 million (10M; A3, A6, B3, B6) triangles. Grayscale images are composed of empty pores (black objects) and solid material (gray objects). Binary images are composed of empty pores (white) and solid material (black).

DISCUSSION

The comparison between morphological characteristics of replicated small prototypes (M_{small} and C_{small}) showed that 3D printing technology was able to retain the basic features of the macropore network. More specifically, the pore size and shape characteristics of the largest pores were easily visualized on the microCT imaging (Fig. 4), highlighting the similarity between reconstructed models. Moreover, introducing some smoothing of the surface walls by the simplification of the mesh (500k vs. 10M triangles) did not show significant changes between macropore characteristics. In particular, the M microCT porosity and pore surface/volume ratio had a coefficient of variation of 3.6 and 4.8%, respectively. These results were supported by others: Otten et al. (2012) reported a very high reproducibility of 12 prototypes since the measured porosity (0.66) was characterized by a very low coefficient of variation (3.36%), although their soil-like prototypes were scaled up three times with respect to the original size of the soil samples. By contrast, our prototypes were reconstructed at the real size, although the soil microscale heterogeneity that was provided by the fine silt and clay particles could not be faithfully reproduced due to the microCT soil scanning (40 μm) and 3D printing resolution limits (29 μm).

The successful reproduction of generated M_{small} prototypes (Fig. 1, Step E) was partly reappraised by evaluating the pore morphological characteristics in detail (Table 2). In fact, the pore structure parameters varied between the reconstructed models,

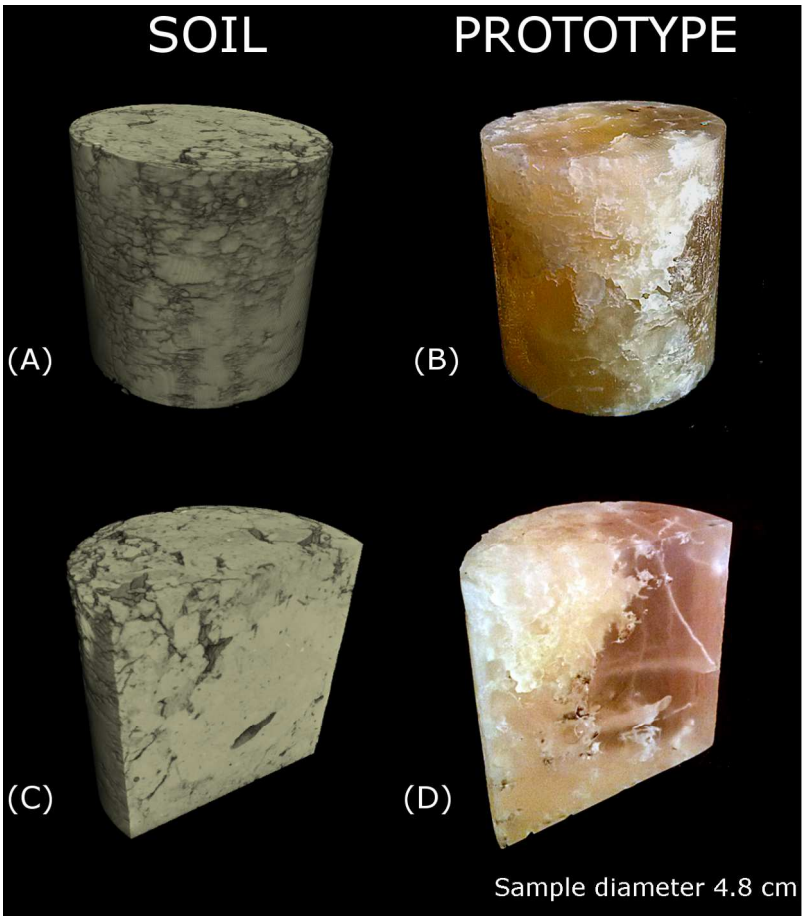

Fig. 5. Three-dimensional representations of a large soil sample (farmyard manure treatment) as a result of X-ray computed microtomography (microCT) analysis (A, C; spatial resolution of 40 μm) and pictures of its 3D-printed copy (B, D; spatial resolution of 29 μm).

especially in the C_{small} prototypes. For instance, the coefficient of variation of total porosity was 11.5% in the C_{small} prototypes, increasing to 63% in the Euler number. Nevertheless, it is worth noticing that the microCT scanning of small prototypes (Fig. 1, Step F) was performed at a resolution (27 μm) that was finer than that used during the 3D-printing (29 μm, ± 50 μm), emphasizing the systematic errors during the model building process. As a result, the mismatch observed between soil samples (M_{soil} and C_{soil}) and prototypes (M_{small} and C_{small}) structures were the result of the combined effect between: (i) soil digital imaging due to microCT scanning; (ii) inaccuracy during the 3D printing process; (iii) prototype digital imaging due to microCT scanning. Furthermore, the 3D mesh generation created distorted elements from the voxel-based microCT volumes, although the negligible variations between small prototypes as printed from 500k and 10M triangles suggested their minor role during the prototypes production. Moreover, the partial effectiveness of wax removal from the macropores (Fig. 4), quantified at around 2.4% (M_{small}) and 16.7% (C_{small}) of microCT porosity, increased the uncertainty on the pore quantity and morphology. Finally, the biggest differences were observed in terms of Euler number, showing its ability to identify slight structure changes between replicated prototypes. The wax entrapped in the voids created a discontinuity between adjacent pores by modifying the degree of connection of the macropore network and partly isolating them from the space outside the solid matrix. As a result, the soil volumes (M_{soil} and C_{soil}) generally had both a higher microCT total porosity and a lower Euler number (i.e., more connections) than the reconstructed prototypes (Table 2). As suggested by the PSD analysis, the wax was easily removed from the largest pores, while it consistently remained in the smallest ones (Fig. 3). Finally, a mismatch between soil and soil-like porosity was probably introduced during microCT soil analysis and the following mesh generation. Indeed microCT imaging was composed of cubic voxels while polygonal mesh comprised a surface triangulation, avoiding their full overlap.

Table 3. Experimental saturated conductivity values ($K_{s\text{-}large}$, m s^{-1}) estimated on soil-like prototypes (M_{large} and C_{large}, 4.8 cm high × 4.8 cm diam.) and compared with experimental ($K_{s\text{-}soil}$) and modeled (K_{Morph}) ones on the original soil samples. Standard error values are reported in brackets.

ID	Replicate	$K_{s\text{-}large}$	$K_{s\text{-}soil}$†	K_{Morph}†
			10^{-6} m s^{-1}	
M	1	134.94	6.31	5.17
M	2	19.46	2.41	4.13
M	3	30.50	3.41	1.74
Average		61.63 (36.79)	4.04 (1.17)	3.68 (1.02)
C	1	N/A	5.27	0.04
C	2	0.23	2.22	0.16
C	3	0.47	1.90	0.24
Average		0.35(0.12)	3.13(1.07)	0.15(0.06)

†data from Dal Ferro et al. (2015).

In spite of the difficulty in totally cleaning the wax from the macropores, measurements of saturated hydraulic conductivity were successfully conducted on five of the six large prototypes. Only the saturated conductivity measurement on one C_{large} prototype failed. Since one of the C_{large} soil-derived model was characterized by the lowest total porosity (0.015), most likely the entrapped wax occluded the scarce conductive pores within the whole prototype and prevented flow. Water flow measurements, calculated through the one interconnected macropore network that spanned the sample, were highly correlated with properties calculated on the original samples ($K_{s\text{-}soil}$) and particularly with those modeled (K_{Morph}) on the same pore network (Fig. 6) (Dal Ferro et al., 2015). Nevertheless, $K_{s\text{-}large}$ had higher values than $K_{s\text{-}soil}$ and K_{Morph} by at least one order of magnitude in the M treatment (Table 3), although the total porosity had been reduced with respect to the soil sample ones in two ways: 1. The prototypes were reconstructed on the basis of digital imaging from microCT scanning that performed at a resolution that excluded all the small connections between the largest pores and decreased the adsorption along the macropore walls; 2. Part of microCT porosity was probably still filled with wax during $K_{s\text{-}}$

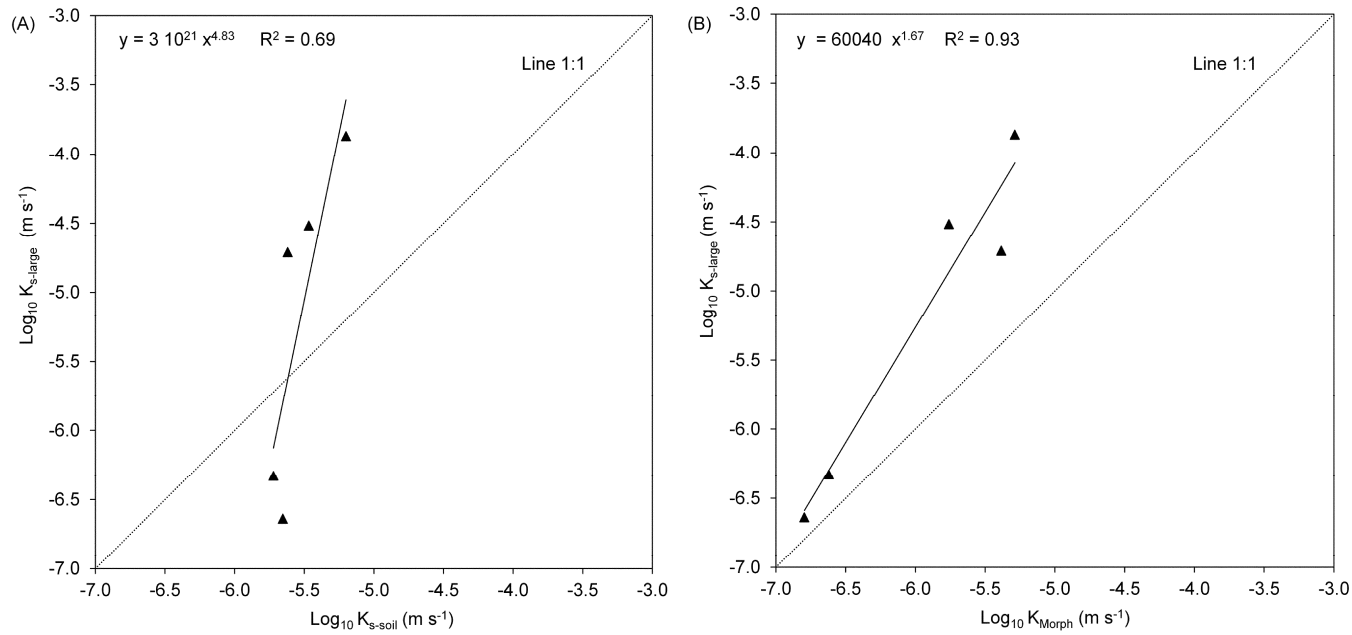

Fig. 6. Relationship between saturated water conductivities estimated on soil-like prototypes ($K_{s\text{-large}}$, m s^{-1}) and on the original soil samples by means of (A) experimental ($K_{s\text{-soil}}$, m s^{-1}) and (B) modeling (K_{Morph}, m s^{-1}) approach.

$_{large}$ measurements, reducing the water flow capacity of the porous medium. These results suggested the major role of conducting macropores on water flow dynamics (Jarvis, 2007), although the undetected and unprinted micropores <80 μm might have partially increased $K_{s\text{-large}}$ to approach the experimental $K_{s\text{-soil}}$ (Elliot et al., 2010), particularly when the soil structure was largely composed of thin pores and microcracks are often insufficiently imaged with microCT and thus underrepresented (i.e., in the control samples), especially in the vicinity of grain contacts (Andrä et al., 2013). Some smoothing of the pore surfaces, introduced during the prototype generation, decreased the friction factor between the liquid and solid phases with respect to the original samples, as was shown by the results of pore surface/volume ratio (Table 2). This would have reduced the pressure drop (Kumar et al., 2011) at high $K_{s\text{-large}}$ values, obeying the dynamics on the viscous forces as described in the Stokes equations, while with low water velocity the difference between $K_{s\text{-large}}$ and $K_{s\text{-soil}}$ and K_{Morph} was strongly reduced. By contrast, the contact angle between the water and the solid walls (69°) was only a minor factor for influencing the water movement, although it is reasonable that, despite the emptying procedure, the pores were still coated with wax that would have induced fluid slip for water flowing over a hydrophobic surface (Tretheway and Meinhart, 2002).

CONCLUSIONS

Integrating X-ray microtomography and 3D printing technology is feasible in soil science at the microscale and provides great opportunities to better understand the role of micro-heterogeneity in the soil-water dynamics. In particular, soil-like prototypes were built with relatively large replicability and similarity to the original ones at the actual size, with a resolution of 80 μm. Moreover, the mesh simplification (from 100M to 500k triangles) did not reveal significant differences between prototypes. By contrast, the full wax removal from the pores was not completely solved as it limited the pore connectivity and increased the surface smoothing. Nevertheless, water conductivity was successfully performed on five of the six large prototypes, showing a strong correlation with experimental and modeled data from the original soil samples. The comparison between $K_{s\text{-large}}$ (i.e., on prototypes) and K_{Morph} (morphologic model) data, performed on the same porous systems, highlighted the major role of the macropore surface smoothing and the hydrophobic nature of wax. In particular, an increase of fluid slip and consequently of water velocity at laminar flow was observed for $K_{s\text{-large}} \geq 10^{-5}$ m s^{-1}, while it was consistently reduced at lower values. By contrast, the detection of micropores < 80 μm would have approached the $K_{s\text{-large}}$ values to reach the experimental ones ($K_{s\text{-soil}}$), especially at low water velocities. To promote a broad application of 3D prototypes in the hydrological research, future application of 3D printing technology should address many technological challenges. In fact a higher microCT scanning and 3D-printed resolution will favor the representation of the soil pore system at the nanoscale and its heterogeneity. Moreover the use of soil-like materials will be able to model the physical-chemical interaction between water and the pore surface. Nevertheless, even at this stage, our work suggests as 3D printing technology can represent a breakthrough technology for the study of soil structure and its interaction with biogeochemical processes.

ACKNOWLEDGMENTS

Part of this research has received funding from the European Union's Horizon 2020 Research and Innovation programme under grant agreement No. 645717 (PROTINUS Project). We are also grateful to Ilaria Piccoli who helped in the microCT digital image analysis and processing of 3D-printed soils.

REFERENCES

Ahuja, L.R., L. Ma, and D.J. Timlin. 2006. Trans-disciplinary soil physics research critical to synthesis and modeling of agricultural systems. Soil Sci. Soc. Am. J. 70:311–326. doi:10.2136/sssaj2005.0207

Andrä, H., N. Combaret, J. Dvorkin, E. Glatt, J. Han, M. Kabel, Y. Keehm, F. Krzikalla, M. Lee, and C. Madonna. 2013. Digital rock physics benchmarks–Part II: Computing effective properties. Comput. Geosci. 50:33–43. doi:10.1016/j.cageo.2012.09.008

Baveye, P.C., D. Rangel, A.R. Jacobson, M. Laba, C. Darnault, W. Otten, R. Radulovich, and F.A.O. Camargo. 2011. From dust bowl to dust bowl: Soils are still very much a frontier of science. Soil Sci. Soc. Am. J. 75:2037–2048. doi:10.2136/sssaj2011.0145

Bacher, M., A. Schwen, and J. Koestel. 2015. Three-dimensional printing of macropore networks of an undisturbed soil sample. Vadose Zone J. 14:10.2136/vzj2014.08.0111

Blunt, M.J., B. Bijeljic, H. Dong, O. Gharbi, S. Iglauer, P. Mostaghimi, A. Paluszny, and C. Pentland. 2013. Pore-scale imaging and modelling. Adv. Water Resour. 51:197–216. doi:10.1016/j.advwatres.2012.03.003

Burdine, N.T. 1953. Relative permeability calculations from pore size distribution data. J. Pet. Technol. 5:71–78. doi:10.2118/225-G

Cnudde, V., and M.N. Boone. 2013. High-resolution X-ray computed tomography in geosciences: A review of the current technology and applications. Earth Sci. Rev. 123:1–17. doi:10.1016/j.earscirev.2013.04.003

Dal Ferro, N., P. Charrier, and F. Morari. 2013. Dual-scale micro-CT assessment of soil structure in a long-term fertilization experiment. Geoderma 204:84–93. doi:10.1016/j.geoderma.2013.04.012

Dal Ferro, N., A.G. Strozzi, C. Duwig, P. Delmas, P. Charrier, and F. Morari. 2015. Application of smoothed particle hydrodynamics (SPH) and pore morphologic model to predict saturated water conductivity from X-ray CTimaging in a silty loam Cambisol. Geoderma 255:27–34. doi:10.1016/j.geoderma.2015.04.019

Downie, H., N. Holden, W. Otten, A.J. Spiers, T.A. Valentine, and L.X. Dupuy. 2012. Transparent soil for imaging the rhizosphere. PLoS ONE 7:e44276. doi:10.1371/journal.pone.0044276

Elliot, T.R., W.D. Reynolds, and R.J. Heck. 2010. Use of existing pore models and X-ray computed tomography to predict saturated soil hydraulic conductivity. Geoderma 156:133–142. doi:10.1016/j.geoderma.2010.02.010

FAO-UNESCO. 1990. Soil map of the world. Revised legend. FAO, Rome.

Feeney, D.S., J.W. Crawford, T. Daniell, P.D. Hallett, N. Nunan, K. Ritz, M. Rivers, and I.M. Young. 2006. Three-dimensional microorganization of the soil–root–microbe system. Microb. Ecol. 52:151–158. doi:10.1007/s00248-006-9062-8

Hsieh, J. 2009. Computed tomography: Principles, design, artifacts, and recent advances. 2nd ed. SPIE, Bellingham, WA.

Hunt, A.G., R.P. Ewing, and R. Horton. 2013. What's wrong with soil physics? Soil Sci. Soc. Am. J. 77:1877–1887. doi:10.2136/sssaj2013.01.0020

Jarvis, N.J. 2007. A review of non-equilibrium water flow and solute transport in soil macropores: Principles, controlling factors and consequences for water quality. Eur. J. Soil Sci. 58:523–546. doi:10.1111/j.1365-2389.2007.00915.x

Ju, Y., H. Xie, Z. Zheng, J. Lu, L. Mao, F. Gao, and R. Peng. 2014. Visualization of the complex structure and stress field inside rock by means of 3D printing technology. Chin. Sci. Bull. 59:5354–5365. doi:10.1007/s11434-014-0579-9

Kumar, V., M. Paraschivoiu, and K.D.P. Nigam. 2011. Single-phase fluid flow and mixing in microchannels. Chem. Eng. Sci. 66:1329–1373. doi:10.1016/j.ces.2010.08.016

Luo, L., H. Lin, and S. Li. 2010. Quantification of 3-D soil macropore networks in different soil types and land uses using computed tomography. J. Hydrol. 393:53–64. doi:10.1016/j.jhydrol.2010.03.031

Mooney, S.J., C. Morris, and P.M. Berry. 2006. Visualization and quantification of the effects of cereal root lodging on three-dimensional soil macrostructure using X-ray computed tomography. Soil Sci. 171:706–718. doi:10.1097/01.ss.0000228041.03142.d3

Mooney, S.J., T.P. Pridmore, J. Helliwell, and M.J. Bennett. 2012. Developing X-ray computed tomography to non-invasively image 3-D root systems architecture in soil. Plant Soil 352:1–22. doi:10.1007/s11104-011-1039-9

Morari, F., E. Lugato, A. Berti, and L. Giardini. 2006. Long-term effects of recommended management practices on soil carbon changes and sequestration in north-eastern Italy. Soil Use Manage. 22:71–81. doi:10.1111/j.1475-2743.2005.00006.x

Mualem, Y. 1976. A new model for predicting the hydraulic conductivity of unsaturated porous media. Water Resour. Res. 12:513–522. doi:10.1029/WR012i003p00513

Otten, W., R. Pajor, S. Schmidt, P.C. Baveye, R. Hague, and R.E. Falconer. 2012. Combining X-ray CT and 3D printing technology to produce microcosms with replicable, complex pore geometries. Soil Biol. Biochem. 51:53–55. doi:10.1016/j.soilbio.2012.04.008

Peat, D.M.W., G.P. Matthews, P.J. Worsfold, and S.C. Jarvis. 2000. Simulation of water retention and hydraulic conductivity in soil using a three-dimensional network. Eur. J. Soil Sci. 51:65–79. doi:10.1046/j.1365-2389.2000.00294.x

Perret, J.S., S.O. Prasher, and A.R. Kacimov. 2003. Mass fractal dimension of soil macropores using computed tomography: From the box-counting to the cube-counting algorithm. Eur. J. Soil Sci. 54:569–579. doi:10.1046/j.1365-2389.2003.00546.x

Rajaram, H., L.A. Ferrand, and M.A. Celia. 1997. Prediction of relative permeabilities for unconsolidated soils using pore-scale network models. Water Resour. Res. 33:43–52. doi:10.1029/96WR02841

Rangel, D.P., C. Superak, M. Bielschowsky, K. Farris, R.E. Falconer, and P.C. Baveye. 2013. Rapid prototyping and 3-D printing of experimental equipment in soil science research. Soil Sci. Soc. Am. J. 77:54–59. doi:10.2136/sssaj2012.0196n

Remy, E., and E. Thiel. 2002. Medial axis for chamfer distances: Computing look-up tables and neighbourhoods in 2D or 3D. Pattern Recognit. Lett. 23:649–661. doi:10.1016/S0167-8655(01)00141-6

Reynolds, W.D., D.E. Elrick, E.G. Youngs, A. Amoozegar, H.W.G. Booltink, and J. Bouma. 2002. Saturated and field-saturated water flow parameters. In: J.H. Dane and G.C. Topp, editors, Methods of soil analysis. Part 4. SSSA, Madison, WI. p. 797–801.

Ringeisen, B.R., K. Rincon, L.A. Fitzgerald, P.A. Fulmer, and P.K. Wu. 2015. Printing soil: A single-step, high-throughput method to isolate micro-organisms and near-neighbour microbial consortia from a complex environmental sample. Methods Ecol. Evol. 6:209–217. doi:10.1111/2041-210X.12303

Serra, J. 1982. Image analysis and mathematical morphology. Academic Press, London.

Tippkoetter, R., T. Eickhorst, H. Taubner, B. Gredner, and G. Rademaker. 2009. Detection of soil water in macropores of undisturbed soil using microfocus X-ray tube computerized tomography (μCT). Soil Tillage Res. 105:12–20. doi:10.1016/j.still.2009.05.001

Tretheway, D.C., and C.D. Meinhart. 2002. Apparent fluid slip at hydrophobic microchannel walls. Phys. Fluids 14:L9–L12. doi:10.1063/1.1432696

Vogel, H.J., U. Weller, and S. Schlüter. 2010. Quantification of soil structure based on Minkowski functions. Comput. Geosci. 36:1236–1245. doi:10.1016/j.cageo.2010.03.007